

Fast, scalable, and interactive software for Landau-de Gennes numerical modeling of nematic topological defects

Daniel M. Sussman^{1,2*} and Daniel A. Beller^{3*}

¹ Syracuse University, Department of Physics, Syracuse, NY, USA

² Emory University, Department of Physics, Atlanta, GA, USA

³ University of California, Merced, Department of Physics, Merced, CA, USA

Correspondence*:

Daniel M. Sussman, Daniel A. Beller

daniel.m.sussman@emory.edu, dbeller@ucmerced.edu

2 ABSTRACT

3 Numerical modeling of nematic liquid crystals using the tensorial Landau-de Gennes (LdG)
4 theory provides detailed insights into the structure and energetics of the enormous variety of
5 possible topological defect configurations that may arise when the liquid crystal is in contact with
6 colloidal inclusions or structured boundaries. However, these methods can be computationally
7 expensive, making it challenging to predict (meta)stable configurations involving several colloidal
8 particles, and they are often restricted to system sizes well below the experimental scale. Here
9 we present an open-source software package that exploits the embarrassingly parallel structure
10 of the lattice discretization of the LdG approach. Our implementation, combining CUDA/C++ and
11 OpenMPI, allows users to accelerate simulations using both CPU and GPU resources in either
12 single- or multiple-core configurations. We make use of an efficient minimization algorithm, the
13 Fast Inertial Relaxation Engine (FIRE) method, that is well-suited to large-scale parallelization,
14 requiring little additional memory or computational cost while offering performance competitive
15 with other commonly used methods. In multi-core operation we are able to scale simulations up to
16 supra-micron length scales of experimental relevance, and in single-core operation the simulation
17 package includes a user-friendly GUI environment for rapid prototyping of interfacial features
18 and the multifarious defect states they can promote. To demonstrate this software package,
19 we examine in detail the competition between curvilinear disclinations and point-like hedgehog
20 defects as size scale, material properties, and geometric features are varied. [We also study the](#)
21 [effects of an interface patterned with an array of topological point-defects.](#)

22 **Keywords:** Landau-de Gennes modeling, nematic, topological defect, numerical modeling, GPGPU

1 INTRODUCTION

23 Nematic liquid crystals' combination of fluidity and orientational order both underlies nematics' widespread
24 technological applications and endows them with topological defects, localized breakdowns in the
25 orientational order stabilized by the medium's broken symmetries. The topological defects of nematics
26 have been integral to the study of liquid crystals since the field's infancy [1].

27 Besides their role as tabletop physical realizations of profound topological ideas, nematic topological
 28 defects – **including disclination lines, point-like hedgehogs, and surface-bound boojums** – are of great
 29 interest for their importance in nematic colloidal suspensions [2]. These composite materials, formed
 30 by suspensions of colloidal particles or nanoparticles in nematics, promise new routes to directed self-
 31 assembly and self-organization. Nanoparticles in nematics are pushed by elastic forces to assemble in
 32 pre-existing defect lines, meaning that sculpted disclinations provide a path to controlled nanoparticle
 33 assembly. Applications include plasmonic properties for metamaterials [3, 4], molecular self-assembly [5],
 34 and quantum-dot assembly in microshells [6, 7]. Even greater complexity arises in the cases of colloidal
 35 particles in the size range of tens of nanometers to several microns, which often have companion topological
 36 defects and which interact through forces mediated by nematic elasticity. Self-assembled structures of
 37 colloidal particles with companion defects include bound pairs, chains [2, 8] and triclinic 3D crystals [9];
 38 with the aid of laser tweezers, other configurations such as 3D crystals with tetragonal symmetry [10]
 39 and sophisticated disclination knots [11, 12, 13, 14] can be stabilized. Tailored self-assembled colloidal
 40 structures hold promise as optical metamaterials for photonics applications, such as photonic bandgap
 41 crystals and microlasers [15, 16, 17, 18].

42 Nematic defect configurations can also be controlled by nontrivial boundary surfaces [19]. Substrate
 43 patterning strategies include topographic variations such as “lock-and-key” docking sites for colloidal
 44 particles [20, 21, 22] and chemical patterning where the boundary condition shifts abruptly [23, 24].
 45 Complex director fields, including disclinations, can be prescribed on a substrate by photoalignment
 46 [25] or by scribing with an atomic force microscope [26]. Confinement in geometries such as capillaries
 47 [27], droplets [28], shells [29], and thin films [30] produces a wealth of point- and line-defect behaviors
 48 stabilized by topology and energetics.

49 The rapidly expanding variety of experimentally created **nematic defect** configurations has benefited
 50 greatly from the understanding provided by robust modeling approaches. One set of approaches is based
 51 on the Frank-Oseen elastic free energy, which penalizes deformations of the nematic director $\hat{n}(\mathbf{x})$, and
 52 which in its simplest form reads

$$\mathcal{F}_{\text{FO}}^{(1)} = \frac{K}{2} \int dV \sum_{i,j=1}^3 (\partial_i n_j)^2. \quad (1)$$

53 The superscript (1) refers to the approximation of a single elastic constant K in this expression. However,
 54 the $\hat{n} = -\hat{n}$ symmetry of nematics presents challenges for this model in the presence of disclinations with
 55 half-integer winding number, especially if their locations are not known beforehand.

56 This difficulty is resolved by the Landau-de Gennes (LdG) model, the theoretical approach which is the
 57 focus of this work and which we review in Sec. 2. The LdG framework takes as its order parameter the
 58 second-rank traceless nematic order tensor $Q_{ij}(\mathbf{x})$, and is well-suited to modeling arbitrary disclination
 59 configurations, as well as biaxial nematics and the blue phases [15, 31]. While little is known analytically
 60 about free energy minimizers in LdG theory in **any but the simplest geometries** [32, 33], numerical
 61 minimization of the LdG free energy has been fruitfully applied over a wide range of systems [10, 11,
 62 12, 15, 34, 35, 36, 37, 38, 39, 40, 41, 42, 43, 44, 45, 21, 46, 47, 48]. Additionally, flow dynamics of
 63 nematics, including active nematic systems, can be modeled by supplementing the LdG free energy with
 64 hydrodynamical equations **as formulated by Beris and Edwards** [49] or by Qian and Sheng [50] and solved
 65 **by methods such as lattice Boltzmann** [51, 52, 53, 54, 55], multiparticle collision dynamics and related
 66 off-lattice methods [56, 57, 58], or finite difference and finite element approaches [59, 60]. Some methods

67 incorporate a fast relaxation of the momentum compared to the director, to account for the separation in
68 time scales for these relaxations in typical molecular liquid crystals [61, 52].

69 The broad usefulness of the LdG theory goes hand in hand with a significant limitation of scale: Resolving
70 defects at *a priori* unknown locations requires the simulation lattice spacing to be comparable to or smaller
71 than the size of the defect core, the region in which nematic order breaks down, which in thermotropic
72 nematics is typically a few nanometers. This is often thousands of times smaller than the individual
73 micron-scale colloidal particles of interest. Therefore, a faithful rescaling of the experimental system in
74 numerics would require of order at least 10^9 lattice sites even for configurations involving only a small
75 number of such colloids.

76 Accessing such experimentally relevant lattice sizes presents computational challenges not often seen
77 in the simulations of glassy and polymeric soft matter systems. The demands on system memory quickly
78 become prohibitive: simply maintaining the five independent degrees of freedom at each lattice site and
79 storing the necessary change in those variables from one minimization step to the next at 10^9 lattice sites
80 requires 80 GB – more than on most current commodity desktops and larger than the memory capacity
81 of any CUDA-capable GPU¹. Additionally, there is a large direct computational cost of even simple
82 manipulations acting on so many degrees of freedom; this contributes to the significant wall-time required
83 for most numerical energy minimizations and presents challenges for efficient exploration of parameter
84 spaces and colloidal particle positions.

85 Consequently, LdG numerical modeling is typically applied to systems significantly scaled down, with
86 respect to a fixed defect core size, as compared with the experiments that they are intended to model. While
87 important qualitative insights about defects and director fields can often be obtained by scaling down the
88 experimental dimensions, the change in size ratios makes quantitative prediction challenging. There can
89 also be major qualitative differences. The most well-known of these is the form of the companion defect to
90 a particle with homeotropic (normal) anchoring: Micron-scale particles typically have hyperbolic hedgehog
91 companions (in the absence of confinement or external fields) [2], whereas particles in the few hundred nm
92 or smaller size range have disclination loops in the “Saturn ring” configuration [62, 63]. This constitutes
93 a major challenge in modeling systems with multiple colloid-hedgehog pairs. Experimental work on
94 high-aspect ratio colloidal particle shapes observes both hedgehogs and disclination loops, but numerical
95 modeling has been limited to the line defect case [35, 64, 65, 65, 42, 40, 41, 38, 43, 39]. Adaptive mesh
96 refinement in finite-element simulations can help to avoid computational and memory expense in regions
97 not near defects [66] but typically does not remove the need to scale down.

98 In this work we present an open-source finite difference-based implementation of LdG free energy
99 minimization with nontrivial boundary conditions, “*openQmin*” [67], using a combination of approaches
100 designed to address the challenges described above. It is written for heterogeneous CPU and GPU operation
101 to target two complementary research goals. First, it offers a user-friendly GUI environment for rapid
102 prototyping of topological defect configurations as a function of liquid crystal parameters, boundary
103 geometry, and the presence of colloidal inclusions. Simultaneously, it targets large-scale systems using
104 OpenMPI [68] to support parallelization across both CPU and GPU resources to scale up to the supra-
105 micron length scales of experimental relevance. We employ efficient minimization algorithms, such as
106 the Fast Inertial Relaxation Engine (FIRE) method, to maintain reasonable convergence times even for
107 large-scale parallelized calculations.

¹ As of July, 2019

108 The remainder of the paper is structured as follows. We begin with a review of the LdG theory in Section
 109 2. Section 3 lays out our numerical approach, first discretizing the LdG theory for a finite-difference method,
 110 and then outlining our use of minimization algorithms and OpenMPI parallelization. In Sec. 4 we present
 111 two sample studies demonstrating the effectiveness of this approach. We first perform a classic analysis of
 112 the companion defects to homeotropic spherical particles at varying system sizes, and then examine the
 113 effects of a boundary patterned with surface disclinations in a supra-micron-scale system. Section 5 briefly
 114 describes the GUI version of *openQmin* with an example of the rapid prototyping workflow it enables.
 115 Finally, in Section 6, we discuss both the range of use we foresee for *openQmin* and some future directions
 116 for additional physics that could be studied in this framework.

2 LANDAU DE-GENNES THEORY FOR NEMATIC LIQUID CRYSTALS

117 Here we give a brief overview of those aspects of the LdG theory used in our numerical approach. The
 118 theory is of course well-established [69] and its use in a finite difference numerical free energy minimization
 119 scheme is described in several sources; the reader is directed to Ref. [47] for a thorough explanation.

120 Uniaxial nematic liquid crystals are characterized by orientational ordering of nematogens (molecules or
 121 suspended anisotropic particles) along a director, \hat{n} , which is a unit vector with the identification $\hat{n} = -\hat{n}$. To
 122 respect that symmetry consistently, which is important at disclinations of half-integer winding number, we
 123 take as order parameter not a director but a second-rank tensor. This is the traceless, symmetric tensor field
 124 $\mathbf{Q}(\mathbf{x})$, whose lattice discretization is the fundamental object of the LdG modeling approach. \mathbf{Q} is related to
 125 \hat{n} by [70]

$$Q_{\alpha\beta} = \frac{3}{2}S \left(n_\alpha n_\beta - \frac{1}{3}\delta_{\alpha\beta} \right) + \frac{1}{2}S_B(m_\alpha m_\beta - l_\alpha l_\beta). \quad (2)$$

126 Here, S is the degree of uniaxial nematic order, and S_B is the degree of biaxial order distinguishing a
 127 preferred direction $\hat{m} \equiv -\hat{m}$, perpendicular to \hat{n} , from $\hat{l} \equiv \hat{n} \times \hat{m}$. The nematic director can be recovered
 128 as the eigenvector corresponding to the largest eigenvalue of \mathbf{Q} , which equals S . Most nematics are uniaxial,
 129 so the equality $S_B = 0$ is true in the absence of distortions and represents a good approximation away from
 130 defects. In this uniaxial limit, Eq. 2 reduces to

$$Q_{\alpha\beta} = \frac{3}{2}S \left(n_\alpha n_\beta - \frac{1}{3}\delta_{\alpha\beta} \right). \quad (3)$$

131 2.1 Phenomenological free energy density

132 The LdG theory constructs a phenomenological free energy \mathcal{F} as a functional of $\mathbf{Q}(\mathbf{x})$. We can write this
 133 functional schematically as [47, 70]:

$$\mathcal{F}[\mathbf{Q}] = \int_V (f_{\text{bulk}} + f_{\text{distortion}} + f_{\text{external}}) dv + \sum_\alpha \int_{S_\alpha} (f_{\text{boundary}}^\alpha) ds \quad (4)$$

134 The first integral, over the volume of the nematic, has three free energy density terms incorporating
 135 respectively the energetic costs arising from deviations away from the thermodynamically preferred degree
 136 of nematic order $S = S_0$, from elastic distortions, and from external fields. The second integral, summing
 137 over all boundary surfaces S_α in contact with the nematic, incorporates the anchoring energy associated

138 with each interface, including the surfaces of colloidal particles; its form may be different for different
 139 surfaces. We address each component in turn:

140 2.1.1 Bulk free energy

141 The first free energy density term in Eq. 4 gives a Landau free energy for the isotropic-nematic phase
 142 transition, written in terms of rotational invariants of \mathbf{Q} in a Taylor expansion about the isotropic, $\mathbf{Q} = 0$
 143 state [71]:

$$f_{\text{bulk}} = \frac{A}{2} \text{tr}(\mathbf{Q}^2) + \frac{B}{3} \text{tr}(\mathbf{Q}^3) + \frac{C}{4} (\text{tr}(\mathbf{Q}^2))^2. \quad (5)$$

144 The parameter $A \propto (T - T_{NI}^*)$, where T_{NI}^* is the temperature at which the isotropic phase is destabilized.

145 In the uniaxial limit f_{bulk} becomes a polynomial in the degree of order,

$$f_{\text{bulk}} = \frac{3}{4} AS^2 + \frac{1}{4} BS^3 + \frac{9}{16} CS^4, \quad (6)$$

146 which is minimized either by $S = 0$ or by

$$S = S_0 \equiv \frac{-B + \sqrt{B^2 - 24AC}}{6C}. \quad (7)$$

147 In the nematic phase, the absolute value of

$$f_0 \equiv f_{\text{bulk}}(S = S_0) \quad (8)$$

148 provides a free energy penalty per unit volume to the melted cores of defects, where $S \rightarrow 0$.

149 2.1.2 Distortion free energy

150 The distortion free energy density models the elasticity of the nematic phase, and represents the LdG
 151 counterpart to the Frank-Oseen free energy density. The latter, in full generality up to second derivatives of
 152 \hat{n} , is

$$\begin{aligned} f_{\text{FO}} = & \frac{1}{2} \{ K_1 (\nabla \cdot \hat{n})^2 + K_2 (\hat{n} \cdot (\nabla \times \hat{n}) + q_0)^2 + K_3 |(\hat{n} \cdot \nabla) \hat{n}|^2 \\ & + K_{24} \nabla \cdot [(\hat{n} \cdot \nabla) \hat{n} - \hat{n} (\nabla \cdot \hat{n})] \}. \end{aligned} \quad (9)$$

153 The parameters in this expression are the splay (K_1), twist (K_2), bend (K_3), and saddle-splay (K_{24}) elastic
 154 constants, and the spontaneous chiral wavenumber q_0 which is nonzero in the cholesteric and blue phases.
 155 Other common conventions for the saddle-splay energy density replace K_{24} in Eq. 9 by either $2K_{24}$ or
 156 $2(K_2 + K_{24})$. Eq. 9 reduces to Eq. 1 under the “one-constant approximation” $K_1 = K_2 = K_3 = K_{24} \equiv K$
 157 and $q_0 = 0$. The one-constant approximation is a reasonable simplification for many molecular liquid
 158 crystals, where K_1 , K_2 , and K_3 typically differ by less than a factor of 5 [72, 73].

159 The most general form of $f_{\text{distortion}}$ that we employ, following Refs. [74, 48, 70], includes all gradient
 160 terms of quadratic order in \mathbf{Q} allowed by symmetry, plus one term at cubic order:

$$\begin{aligned} f_{\text{distortion}} = & \frac{L_1}{2} \frac{\partial Q_{ij}}{\partial x_k} \frac{\partial Q_{ij}}{\partial x_k} + \frac{L_2}{2} \frac{\partial Q_{ij}}{\partial x_j} \frac{\partial Q_{ik}}{\partial x_k} + \frac{L_3}{2} \frac{\partial Q_{ik}}{\partial x_j} \frac{\partial Q_{ij}}{\partial x_k} \\ & + \frac{L_4}{2} \epsilon_{lik} Q_{lj} \frac{\partial Q_{ij}}{\partial x_k} + \frac{L_6}{2} Q_{lk} \frac{\partial Q_{ij}}{\partial x_l} \frac{\partial Q_{ij}}{\partial x_k}, \end{aligned} \quad (10)$$

161 where Einstein summation over repeated indices is implied, and ϵ is the Levi-Civita tensor. Equation 10
 162 corresponds in the uniaxial limit to Eq. 9 with the identifications [48]

$$\begin{aligned} L_1 &= \frac{2}{27S^2} (K_3 - K_1 + 3K_2), \\ L_2 &= \frac{4}{9S^2} (K_1 - K_{24}), \\ L_3 &= \frac{4}{9S^2} (K_{24} - K_2), \\ L_4 &= -\frac{8}{9S^2} q_0 K_2, \\ L_6 &= \frac{4}{27S^3} (K_3 - K_1). \end{aligned}$$

163 The one-constant approximation in the absence of spontaneous chiral ordering sets $L_2 = L_3 = L_4 =$
 164 $L_6 = 0$, leaving the much simpler and more computationally efficient form

$$f_{\text{distortion}}^{(1)} = \frac{L_1}{2} \frac{\partial Q_{ij}}{\partial x_k} \frac{\partial Q_{ij}}{\partial x_k}, \quad (11)$$

165 which corresponds in the uniaxial limit to Eq. 1 with $L_1 = 2/(9S^2)K$.

166 Taking this simpler form of the distortion energy density, we estimate the defect core size by considering
 167 a distorted uniaxial nematic configuration at $S = S_0$ with \hat{n} varying with typical gradient $1/\ell$. Roughly
 168 speaking, the energy well depth f_0 (Eq. 8) gives the threshold value for $f_{\text{distortion}}$ at which distortions
 169 become so energetically costly that a local melting of nematic order occurs instead. This length $\ell = \xi_N$,
 170 the nematic correlation length (or coherence length), sets the size of the defect core:

$$\xi_N \sim \sqrt{L_1/|f_0|}. \quad (12)$$

171 2.1.3 External fields free energy

172 The response of the nematic to an external magnetic field \mathbf{H} or an external electric field \mathbf{E} is modeled by
 173 the free energy density term

$$f_{\text{external}} = -\frac{1}{3}\mu_0 H_i \Delta\chi Q_{ij} H_j - \frac{1}{3}\varepsilon_0 E_i \Delta\varepsilon Q_{ij} E_j \quad (13)$$

174 where $\Delta\chi$ and $\Delta\varepsilon$ are the anisotropic parts (difference in principal values corresponding to \hat{n} and its
 175 perpendicular directions) of the magnetic susceptibility tensor and dielectric tensor, respectively [34], and
 176 μ_0 and ε_0 are respectively the magnetic permeability and electric permittivity of free space. (We omit here
 177 the terms for the isotropic parts of these tensors, as they do not couple to \mathbf{Q} .) In the uniaxial limit, the
 178 right-hand side becomes $-\frac{1}{2}S\mu_0\Delta\chi(\mathbf{H} \cdot \hat{n})^2 - \frac{1}{2}S\varepsilon_0\Delta\varepsilon(\mathbf{E} \cdot \hat{n})^2$ (again dropping isotropic terms with no
 179 coupling to \hat{n}). Positive $\Delta\chi$ or $\Delta\varepsilon$ will favor alignment of \hat{n} with \mathbf{H} or \mathbf{E} .

180 2.1.4 Boundary free energy

181 Boundary surfaces, including the surfaces of embedded colloidal particles, generally impose an anchoring
 182 surface energy density f_{boundary} representing the surface tension's dependence on the director at the surface.
 183 In terms of the director, a common modeling choice for the anchoring energy is the Rapini-Papoular form

184 $-\frac{1}{2}W_{\text{RP}}^{\alpha}(\hat{\nu}^{\alpha} \cdot \mathbf{n})^2$ where $\hat{\nu}^{\alpha}$ is the surface normal vector and $|W^{\alpha}|$ is the anchoring strength of surface
 185 α [75]. Homeotropic (normal) anchoring follows from $W_{\text{RP}} > 0$, whereas $W_{\text{RP}} < 0$ creates degenerate
 186 planar anchoring, which equally favors every direction perpendicular to $\hat{\nu}^{\alpha}$. The same anchoring functional
 187 can favor a different anchoring direction, for example an in-plane direction in the case of oriented planar
 188 anchoring, using $W_{\text{RP}} > 0$ with the replacement of $\hat{\nu}^{\alpha}$ by the favored direction.

189 In LdG theory, for homeotropic or other oriented anchoring, the Rapini-Papoular form is generalized as
 190 the Nobili-Durand surface anchoring form [76],

$$f_{\text{boundary}}^{\alpha} = W_{\text{ND}}^{\alpha} \text{tr}((\mathbf{Q} - \mathbf{Q}^0)^2) = W_{\text{ND}}^{\alpha}(Q_{ij} - Q_{ij}^{\alpha})(Q_{ij} - Q_{ij}^{\alpha}), \quad (14)$$

191 where $W_{\text{ND}}^{\alpha} > 0$ is the anchoring strength of surface α and the surface-preferred \mathbf{Q} -tensor, \mathbf{Q}^{α} , is usually
 192 taken to be $Q_{ij}^{\alpha} = \frac{3}{2}S_0(n_i^{\alpha}n_j^{\alpha} - \frac{1}{3}\delta_{ij})$, with $\hat{n}^{\alpha} = \hat{\nu}^{\alpha}$ or some other surface-preferred director.

193 For degenerate planar anchoring, the Nobili-Durand form is not suitable, and we use instead the following
 194 free energy due to Fournier and Galatola [77]:

$$f_{\text{boundary}}^{\alpha} = W_{\text{FG}}^{\alpha}(\tilde{Q}_{ij} - \tilde{Q}_{ij}^{\perp})(\tilde{Q}_{ij} - \tilde{Q}_{ij}^{\perp}), \quad (15)$$

195 where $\tilde{Q}_{ij} = Q_{ij} + S_0\delta_{ij}/2$ and $\tilde{\mathbf{Q}}^{\perp}$ is the projection onto $\hat{\nu}^{\alpha}$ via $\tilde{Q}_{ij}^{\perp} = P_{ik} - \tilde{Q}_{k\ell}P_{\ell j}$ for $P_{ij} =$
 196 $\delta_{ij} - \nu_i^{\alpha}\nu_j^{\alpha}$. Assuming \mathbf{Q} is uniaxial with $S = S_0$, the Rapini-Papoular anchoring is recovered with
 197 $W_{\text{RP}}^{\alpha} = 9S_0^2W_{\text{ND,FG}}^{\alpha}$.

3 NUMERICAL APPROACH

198 3.1 Overview

199 The primary contribution of this work is the presentation of an open-source numerical implementation that
 200 exploits the embarrassingly parallel structure of the lattice discretization of the above phenomenological
 201 theory. Our implementation, combining CUDA/C++ [78] and OpenMPI [68], was written with extreme
 202 flexibility in mind to allow users to accelerate simulations large and small using combinations of available
 203 CPU and GPU resources in either single- or multiple-core configurations.

204 The foundation of the software package, “dDimensionalSimulation,” is a set of generic classes meant
 205 to execute simulations of N interacting units, each consisting of d scalar degrees of freedom, using data
 206 structures appropriate for efficient execution on either CPU or GPU resources. These generic classes
 207 serve as the template for *models* which instantiate the dN total degrees of freedom, *forces* which compute
 208 interactions between degrees of freedom, *updaters* which can change the degrees of freedom (e.g., by
 209 implementing equations of motion), and *simulations* which tie objects of these various types together. The
 210 present work focuses on implementing the details of these classes to carry out lattice-based LdG modeling
 211 to find energy-minimized configurations of equilibrium nematics in the presence of various boundary
 212 conditions. The general structure we have employed was chosen to allow flexibility in future development,
 213 for example to derive new model classes which include not only the \mathbf{Q} -tensor but also density and velocity
 214 degrees of freedom, as would be appropriate for modeling active nematic systems [53, 54, 55, 60].

215 In addition to writing efficient code to carry out the required lattice-based minimizations of the \mathbf{Q} -tensor
 216 field in a domain, we also advocate the use of the graphical user interface (GUI) we developed to rapidly
 217 prototype and explore the effects of particular boundaries, colloidal inclusions, and external fields that
 218 may be of experimental interest. The GUI allows a wide variety of user operations – adding boundary

219 objects at any stage of the simulation, starting and stopping minimization, adding or removing external
 220 fields at will – all while visualizing the resulting defect structure and recording configurational details. A
 221 snapshot of the GUI is shown in Fig. 1, and more details of the available features are given in Sec. 5. We
 222 envision that this capability will allow for rapid prototyping of experimental geometries in the search for
 223 particular controllable defect states; running on a single GPU allows real-time visualization of lattices in
 224 the low-millions of total sites. We have also included several example files that use the code in a non-GUI
 225 mode; these can then use OpenMPI to parallelize across either CPU or GPU resources to scale up to lattices
 226 that represent supra-micron-scale liquid crystal systems.

227 3.2 Lattice discretization and energy minimization

228 The finite difference lattice calculations employed in this work use a regular cubic lattice discretization
 229 of space, with a \mathbf{Q} -tensor defined at each site $\vec{x} = \{x, y, z\}$. The lattice Δx spacing can be related
 230 to physical quantities through a natural nondimensionalization of the free energy density, $\tilde{f} \equiv f/|A|$,
 231 which implies a nondimensionalization of the elastic constants $\tilde{L}_i \equiv L_i/(|A|\Delta x^2)$. In the one-constant
 232 approximation, we thus have $\Delta x^2 = L_1/(\tilde{L}_1|A|)$. In this work we set $\tilde{L}_1 = 2.32$. To model 5CB, following
 233 Ref. [47] we take $A = -0.172 \times 10^6 \text{ J/m}^3$, $B = -2.12 \times 10^6 \text{ J/m}^3$, $C = 1.73 \times 10^6 \text{ J/m}^3$, and
 234 $K = L_1 \cdot 9S_0^2/2 = 1 \times 10^{-11} \text{ N}$ where $S_0 \approx 0.53$. These give a lattice spacing of $\Delta x \approx 4.5 \text{ nm}$, which is
 235 at the few-nm scale of the defect core in 5CB. Note that the nondimensionalization of all constants by an
 236 energy scale $|A|$ and a length Δx is implicitly made for all values in *openQmin*, including in the GUI.

237 The symmetry and tracelessness of \mathbf{Q} leaves five independent degrees of freedom, which we take to
 238 be $\vec{q} \equiv \{Q_{xx}, Q_{xy}, Q_{xz}, Q_{yy}, Q_{yz}\}$ at each of the N lattice sites in the simulation domain. We write the
 239 local free energy density $f(\vec{x})$ in terms of these five independent variables, so that the symmetry and
 240 tracelessness of \mathbf{Q} are automatic (rather than being maintained by projection operations following update
 241 steps [47]). We also label each site with an integer “type,” indicating whether it is a bulk site, a boundary
 242 site, or a site inside an object (for instance, the interior of a colloidal inclusion, or part of a bounding
 243 surface), depending on the geometry of the problem. Only bulk and boundary sites are “simulated sites”,
 244 meaning \mathbf{Q} is defined there.

245 We discretize the total free energy, $\mathcal{F} = \sum_{i=1}^N f(\vec{x}_i)$, using a finite-difference approach over the $5N$
 246 independent variables. For the distortion terms we allow the user to select either the more general expression,
 247 Eq. 10, or the more computationally efficient expression of Eq. 11. For the terms in $f_{\text{distortion}}$ which contain
 248 spatial first derivatives of \mathbf{Q} , we consider first-order forward and backward finite difference approximations,

$$\left(\frac{\partial Q_{ij}}{\partial x_k} \right) (\vec{x}) \approx \begin{cases} Q_{ij}(\vec{x} + \hat{x}_k) - Q_{ij}(\vec{x}) & \text{(forward)} \\ Q_{ij}(\vec{x}) - Q_{ij}(\vec{x} - \hat{x}_k) & \text{(backward).} \end{cases} \quad (16)$$

249 Here \hat{x}_k is the unit vector in the x_k direction, and \vec{x} is the site where the calculation is taking place.
 250 The choice of a regular cubic lattice makes these derivative approximations straightforward to calculate.
 251 The forward and backward finite differences are each compatible with the simulation domain only if
 252 $(\vec{x} + \hat{x}_k)$, $(\vec{x} - \hat{x}_k)$, respectively, are simulated (bulk or boundary) sites. We then take, as the discretized
 253 expression of f , Eq. 4 averaged over all forward and backward finite difference expressions for each of
 254 $k = 1, 2, 3$ that are allowed by the geometry of the simulation domain. A bulk site, therefore, has a local
 255 free energy averaged over 2^3 such combinations, while a boundary site has fewer. We use these averages
 256 over different expressions for the finite differences, rather than using a single centered finite difference
 257 formula $(\partial Q_{ij}/\partial x)(\vec{x}) \approx \frac{1}{2}[Q_{ij}(\vec{x} + \hat{x}_k) - Q_{ij}(\vec{x} - \hat{x}_k)]$, because using the latter form in Eq. 11 produces

258 no terms coupling $Q_{ij}(\vec{x})$ to its nearest neighbors, of the form $Q_{ij}(\vec{x})Q_{ij}(\vec{x} \pm \hat{x}_k)$. This use of the centered
259 first derivative expression would therefore create an artificial (and undesirable) lattice doubling effect in
260 our approach, with even sites and odd sites evolving independently. For curved boundaries such as on
261 spherical colloidal particles, well-known inaccuracies are introduced in the finite difference calculations
262 by the discretization of boundaries as sites in the cubic lattice [79]. Specifically, errors of order $O(\Delta x)$ in
263 $Q_{ij}(\vec{x})$ are introduced, leading to truncation error of $O(1)$ (which do not diverge as the lattice spacing is
264 refined) in the first derivative approximations of Eq. 16.

265 Finally, we minimize \mathcal{F} as a cost function over the $5N$ independent variables $q_i(\vec{x}_j)$, $i = 1, \dots, 5$,
266 $j = 1, \dots, N$. The gradient of \mathcal{F} in this $5N$ -dimensional space is calculated by explicitly differentiating
267 the expression for \mathcal{F} with respect to each $q_i(\vec{x}_j)$ degree of freedom. This explicit differentiation of a cost
268 function is an alternative to the approach of analytically deriving local forces (molecular fields) from the
269 Euler-Lagrange equations, projecting to recover symmetry and tracelessness, and then discretizing those
270 expressions. While the Euler-Lagrange equations have separate forms for the bulk and the boundaries, in
271 the approach used here forces are derived from the cost function in formally the same way for bulk and
272 boundary sites.

273 We emphasize that by discretizing space, we can directly map the problem of solving the LdG partial
274 differential equations to finding the minima of a complex energy landscape (where the Q-tensors on
275 each lattice site are the degrees of freedom). For instance, many PDE solvers implement steepest descent
276 relaxation, which can be directly interpreted as overdamped molecular dynamics at zero temperature. This
277 allows us to turn to the wealth of existing algorithmic approaches from the field of nonlinear optimization,
278 including minimization techniques such as quasi-Newton methods, (conjugate) gradient descent, and
279 momentum-based techniques such as Nesterov's accelerated gradient [80]. Since our aim is to be able
280 to scale up to large systems, we ignore minimizers which require second-order derivatives of the cost
281 function, and we find that even limited-memory quasi-Newton methods such as L-BFGS impose too-strong
282 a memory requirement for many of our purposes. Additionally, while conjugate gradient is appealing in
283 having only marginal extra memory requirements and being much faster than simple gradient descent, it
284 involves frequent line searches that require expensive repeated evaluations of the free energy density and
285 imposes additional parallelization costs.

286 Thus, although we have implemented many of the above-named minimizers in *openQmin*, we focus our
287 attention on the use of the Fast Inertial Relaxation Engine (FIRE) method of energy minimization [81].
288 FIRE falls into the class of “gradient plus momentum”-style minimization algorithms, and it additionally
289 rescales the “velocity” (fictitious additional variables introduced to make the analogy with molecular
290 dynamics even more complete and corresponding to the velocities at which the Q-tensor components
291 change) of the degrees of freedom and adaptively changes the size of the time step itself based on the
292 behavior of the force and velocity during the most recent update. For convex optimization problems
293 the addition of inertia can be proven to enhance convergence [82], although for more complex energy
294 landscapes in general little can be proven. Thus, while it is a heuristic approach, FIRE has been shown to be
295 competitive with (or even faster than) conjugate gradient minimization [81, 83, 84], all while maintaining
296 an extremely light additional memory footprint and being highly amenable to parallelization across multiple
297 cores or multiple GPU units. Note that FIRE was originally developed with atomistic simulations in mind,
298 but it is increasingly being used more generally, including in the solution of PDEs [85] and in machine

299 learning applications [86]. By the straightforward mapping mentioned above we are able to directly apply
 300 the pseudocode presented in Algorithm 1.

```

Initialize Q-tensors at each lattice site, set velocities  $v_i$  to zero;
while Minimization criteria not satisfied do
  Update  $q_i(\vec{x}_j)$ , force  $= -\nabla \mathcal{F}$ , and  $v_i$  using a velocity Verlet step;
  Calculate power,  $P$ , as the dot product of the force and velocity vectors;
  Rescale velocity by a parameter  $\alpha$  which sets the inertia of the degrees of freedom;
  if  $P > 0$  then
    if  $P$  has been positive for more steps than a threshold,  $N_{min}$  then
      | Increase the time step size and increase  $\alpha$ .
    end
  else
    | Decrease the time step size, reset velocities to zero, reset  $\alpha$  to initial value;
  end
end
```

Algorithm 1: Pseudocode for FIRE minimization [81]

302 We first demonstrate this efficient minimization in Fig. 2, where we compare the system energy and
 303 average norm of the force on the degrees of freedom during the minimization of a lattice of $N = 250^3$ sites
 304 in a cubic geometry with periodic boundary conditions. To make a fair comparison, we have performed both
 305 a FIRE and a gradient descent (GD) minimization on the same system using separately tuned minimization
 306 parameters for each algorithm. We use the same hardware for each simulation, and report the minimization
 307 progress in terms of the wall-clock time taken. Although it is sometimes common to report efficiency
 308 in such comparisons in units of function calls, for algorithms with very different numbers of arithmetic
 309 operations (each FIRE iteration requires more than twice the number of arithmetic operations compared to
 310 GD) such comparisons are often misleading.

311 As Fig. 2 makes clear, even in the trivial case of finding the uniform nematic ground state for a system
 312 with no boundary terms from a system initialized with random Q-tensors at each lattice site, FIRE provides
 313 orders of magnitude improvement in the time taken to find minima. This performance of our default
 314 minimizer is not restricted to simple, bulk states of the liquid crystals. As we demonstrate in Fig. 3 for
 315 a handful of simple (and well studied) arrangements of colloidal inclusions and boundaries, FIRE is
 316 very rapidly able to find these more complex minima, too. **As with any non-convex optimization solver,**
 317 **though, no guarantees are made by FIRE about avoiding particular local minima in favor of a true global**
 318 **minimum. Where this is a concern, we adopt the standard approach of minimizing from multiple different**
 319 **random initializations.** Particularly when coupled with a GPU, the substantial acceleration of FIRE-based
 320 minimizations enables the usefulness of the GUI, as the evolution of defect structures in response to
 321 user-instigated changes can be seen in real time.

322 Although numerical simulations of this size have been commonly used to make contact with experiments,
 323 in single-core operation it is impractical to simulate lattices much larger than $N \sim 300^3$, with the limiting
 324 factor being the wall-clock time required for CPUs and memory constraints for GPUs. Given a simulation
 325 with \mathcal{N} degrees of freedom and spreading the work across P processing units (either GPUs or CPUs),
 326 achieving ideal \mathcal{N}/P scaling requires both low-latency communication between processors and algorithms
 327 that are themselves linear in \mathcal{N}/P . Fortunately, lattice-based models with only nearest- and next-nearest-
 328 neighbor interactions are trivial to parallelize using a pattern common to, e.g., spin glasses [87]. **We use a**
 329 **standard spatial decomposition of the total number of lattice sites into rectilinear sub-regions (typically**

330 cubes, although other spatial partitions are easily implemented, and may be preferable for some simulation
 331 geometries). Each processing unit is assigned to one of these subregions, and is responsible for controlling
 332 and updating the lattice sites in that subregion. It also maintains information about the state of the “halo” of
 333 lattice sites that are neighbors, nearest-neighbors, and next-nearest neighbors of lattice sites at the boundary
 334 of the subregion it controls. Standard OpenMPI protocols [68] are used during each simulation step to
 335 communicate information about the state of these halo sites to and from each processing unit in optimized
 336 sequences of uni-directional transfers.

337 We now assess how our method’s efficiency scales as the problem size is increased. Although *strong*
 338 scaling (Amdahl’s law) – in which the total problem size is kept fixed and P is increased – is often
 339 important, it is well-established that the structure of the near-neighbor lattice interactions we simulate is
 340 embarrassingly parallel. Our real aim is to scale up the problem size itself and use many processors to
 341 simulate lattices that approach experimental scales. As such, *weak scaling* (Gustafson’s law) – in which the
 342 amount of work per processing unit is kept constant – is the relevant test.

343 One challenge to mention here is that when targeting energy minima – as opposed to simply advancing
 344 a molecular dynamics simulation for a fixed number of time steps – the number of minimization steps
 345 itself grows with the total system size. In general the convergence properties of different minimizers in
 346 non-convex settings are highly nontrivial. For simple geometries we are able to numerically probe this
 347 scaling – for instance, we find that in the absence of any boundary the number of minimization steps to
 348 achieve a target small force tolerance scales with the linear size of the system, whereas in the presence of a
 349 spherical colloid it scales roughly with $L^{3/2}$. In general, though, the approximate scaling may be hard to
 350 ascertain (and may depend on the target threshold for declaring a configuration to be in a minimum).

351 Turning instead, then, to the per-minimization-step timings, we present the weak scaling performance of
 352 *openQmin* in Fig. 4, where we compute the total number of lattice-site updates (i.e. N times the number of
 353 simulated time steps) during a minimization in which we fix N_p , the number of lattice sites per processing
 354 unit, at several values and vary P . Consistent with a globally cubic simulation, we parallelized across
 355 $P = 1^3, 2^3, 3^3, 4^3, 5^3, 6^3, 7^3, 8^3, 9^3, 10^3$ processors on the Comet XSEDE cluster, and studied
 356 computational performance for $N_p = 75^3, 100^3, 125^3, 150^3, 250^3$. As expected, there are systematic
 357 drops due to increased communication costs as one goes from 1 core to multiple cores to multiple nodes,
 358 but *openQmin* recovers ideal linear scaling of lattice updates with P as P grows very large. Additionally,
 359 there is a systematic degradation of performance for *small* N_p , since in that case there is a more unfavorable
 360 ratio of halo sites to controlled sites for each processor.

361 Note that when we set the characteristic lattice spacing to correspond to 4.5nm, the largest system
 362 simulated in this study, $N_p \times P = (250^3) \times 10^3$, corresponds to a simulation domain of volume $1424 \mu\text{m}^3$.

4 SAMPLE STUDIES

363 4.1 Companion defects to homeotropic spherical colloids

364 In this section we apply *openQmin* to the question of whether a hyperbolic hedgehog or a Saturn ring
 365 disclination loop provides the minimum-energy form of the topological companion defect to a homeotropic
 366 spherical colloid. As mentioned above, a larger colloid radius a favors the dipolar configuration with a
 367 hedgehog, whereas smaller a favors the quadrupolar configuration with a Saturn ring. As a result, the
 368 common rescaling of experimental dimensions to smaller a/ξ_N in numerical modeling risks obtaining
 369 qualitatively different topological defect configurations. Besides increasing the simulation box size, altering

370 the modeled material constants can restore qualitative agreement between experiment and simulation. Here
 371 we explore the issue in detail, using *openQmin* to systematically investigate the stability of hedgehogs
 372 relative to Saturn rings over a range of sizes and material parameters.

373 The dipolar configuration with a hyperbolic hedgehog is the ground state for homeotropic colloidal
 374 particles near or above the micron scale [2]. Terentjev's prediction of the alternative quadrupolar director
 375 field configuration with a Saturn ring disclination loop [62] can be stabilized for large particles by
 376 confinement or external fields [88, 89]. Stark [63] demonstrated numerically using the Frank-Oseen free
 377 energy that the Saturn ring becomes metastable relative to the dipole for $a \lesssim 720$ nm, with a defect core
 378 size $r_c = 10$ nm. For $a \lesssim 270$ nm, the Saturn ring becomes the global ground state.

379 While the elastic energies of the two configurations are complicated to express, the Saturn ring is
 380 additionally penalized by a simple core energy per unit length, or line tension, $\gamma = \pi K/8$ [63, 69]. Because
 381 the Saturn ring maintains a radius r_d just slightly larger than that of the colloidal particle, $r_d \approx 1.1a$ [63],
 382 the total defect core energy penalty $E_c = 2\pi r_d \gamma \propto Kr_d$ of the Saturn ring grows linearly with the colloid
 383 radius. In contrast, the hyperbolic hedgehog has no defect core dimension growing in size with the colloidal
 384 particle, helping to stabilize the dipole over the Saturn ring at larger colloid sizes.

385 In order to numerically model multi-particle configurations in the dipolar size regime – if we cannot
 386 exploit crystal symmetries to obtain a small unit cell [45, 10] – we must either scale up the simulation
 387 volume to larger lattices, or stabilize the dipole at smaller particle sizes. We can achieve the latter by
 388 altering the materials constant ratios $\tilde{B} \equiv B/A$, $\tilde{C} \equiv C/A$ in Eq. 5. Together, these two ratios determine
 389 S_0 via Eq. 7, as well as the nondimensionalized free energy density of the nematic ground state $f_0 \equiv f_0/A$
 390 with the energy well depth f_0 defined as in Eq. 8.

391 By varying \tilde{B} and \tilde{C} such that S_0 remains fixed, we alter the energetic cost per unit volume of melted
 392 nematic order in defect cores, $|f_0|$. The defect core size r_c varies with the nematic correlation length ξ_N ,
 393 which, from Eq. 12, scales as $\sim \sqrt{L_1/|f_0|}$. Thus, an increase in $|f_0|$ implies a decrease in the defect core
 394 size, which means effectively that the ratio a/r_c of the particle size to the defect core size is increased
 395 without changing the size of the simulation lattice. The dipolar configuration is therefore expected to
 396 remain stable at smaller particle sizes. This technique was used in Ref. [37] to model a dynamical transition
 397 from Saturn ring to dipole as a colloidal particle approaches an undulated boundary, at simulation box sizes
 398 up to 50 times smaller than the experimental dimensions.

399 The results of this study are shown in Fig. 5, which we parameterize by varying \tilde{B} at fixed $S_0 = 0.53$
 400 (i.e., setting $\tilde{C} = (2 - \tilde{B}S_0)/(3S_0^2)$), along with the size of the spherical colloid and the lattice size. We
 401 test the stability of hyperbolic hedgehogs by initializing the surrounding lattice sites in the dipolar defect
 402 configuration suggested by Ref. [90], performing an energy minimization, and testing whether the resulting
 403 configuration has remained in the hedgehog state or transitioned to a Saturn ring configuration (thus,
 404 testing the meta-stability of the dipolar defect state as a function of system parameterization). At the values
 405 $\tilde{B} \approx 12$, $\tilde{C} \approx -10$ commonly used in modeling of 5CB [47], we find that the lower limit of hedgehog
 406 metastability is $a \approx 74$ lattice spacings, or about 330 nm. In this sample study we have imposed a large but
 407 finite anchoring strength at the colloid's surface. Weaker anchoring strength will affect the results, with a
 408 “surface ring” configuration replacing the dipole at low anchoring strength [63].

409 We have also tested the meta-stability of the quadrupolar defect configuration by initializing the system
 410 in a Saturn ring configuration and minimizing, but we have not observed the spontaneous appearance of
 411 hedgehog defects from such simulations, indicating at least the meta-stability (if not absolute stability)
 412 of Saturn rings over the entire parameter range studied here. In addition to the effect of defect core size

413 mentioned above, slight deviations in hedgehog meta-stability as a function of lattice size at fixed \tilde{B} and
 414 a seen in Fig. 5 indicate the importance of far-field distortion terms on the (meta-) stability of defect
 415 configurations.

416 4.2 Patterned boundary conditions

417 To demonstrate the modeling of patterned boundaries in *openQmin*, we examine a square array of
 418 alternating ± 1 disclinations imprinted as a spatially varying anchoring direction on a planar substrate. Such
 419 an array was created experimentally by the authors of Ref. [26], by scribing lines into a polyimide surface
 420 with an atomic force microscope. As in that experiment, we give the opposing surface degenerate planar
 421 anchoring. In *openQmin*, these boundary conditions are specified at each boundary lattice site through
 422 a user-prepared text file (see Sec. 5 below). We employ periodic boundary conditions in the horizontal
 423 directions, and the anchoring strength W at both surfaces is set to make the extrapolation length K/W
 424 roughly equal to the lattice spacing.

425 Fig. 6a shows the result of minimizing a cell of thickness $h = 224$ lattice spacings, corresponding to ≈ 1
 426 μm for 5CB, and a spacing d between defects equal to h . We create an 8 by 8 array of defects, so the total
 427 volume modeled is $64 \mu\text{m}^3$, larger than the maximum size achievable with single core minimizations on a
 428 typical CPU ($\approx 10 - 20 \mu\text{m}^3$). Simulating several unit cells of the substrate patterning in this way allows
 429 us to observe a labyrinthine configuration of half-integer disclination lines near the plane of the substrate,
 430 connecting neighboring surface-defects. Meanwhile, some disclination lines are vertical, traveling between
 431 the two surfaces and imprinting a $+\frac{1}{2}$ or $-\frac{1}{2}$ defect profile on the top surface. The stopping condition for
 432 the minimization here was a somewhat modest force tolerance, allowing these large-system-size studies to
 433 be completed in less than 24 hours. While clearly not completely equilibrated, the horizontal disclination
 434 labyrinth is similar to a domain wall texture observed experimentally in Ref. [26], which may also be
 435 kinetically trapped. Absent from the texture in Fig. 6a is the ± 1 non-singular escaped configuration, which
 436 did appear in the experiments.

437 The energetic cost per unit length of disclination lines implies that the vertical configuration is favored by
 438 smaller cell thickness h . Indeed, as shown in Fig. 6b, when we decrease h/d from 1 to $\frac{1}{6}$, only vertical
 439 disclinations appear, in pairs of $+\frac{1}{2}$ or $-\frac{1}{2}$ disclinations from the “splitting” of the ± 1 surface defects. This
 440 defect splitting was sometimes observed in Ref. [26] in place of the escaped configuration. Conversely,
 441 as shown in Fig. 6c, only horizontal disclinations appear when h/d is increased to 2. Extensions to even
 442 larger defect arrays, to curved boundaries, and to spatially nonuniform anchoring types can be explored in
 443 the same manner in *openQmin*.

5 RAPID PROTOTYPING WITH GUI INTERFACE

444 Figure 1 shows a screenshot of the graphical user interface in action, and the supplemental video
 445 and accompanying narrative transcript of the video in the supplemental text shows a representative
 446 demonstration of its use. Here we discuss some of its current functionality. Initialization dialog boxes
 447 allow the user to set the simulation size, the computational resource to use (CPU or GPU, autodetecting
 448 whether CUDA-capable resources are available for use), and parameters for the bulk and distortion free
 449 energy density. This generates a random bulk configuration of \mathbf{Q} -tensor lattice sites with periodic boundary
 450 conditions. For the visualization pane the user can specify the density and magnitude of directors to draw
 451 (taken to be the direction of the largest eigenvector of \mathbf{Q} at each site), and can freely rotate and zoom
 452 in on the configuration, as well as highlight in blue defects defined locally by regions where the largest
 453 eigenvalue of \mathbf{Q} falls below some threshold.

454 In the top left are buttons allowing the user to specify parameters from one of two energy minimization
455 techniques to use (FIRE and Nesterov's Accelerated Gradient Descent); the resulting dialog boxes are
456 populated with values that we typically find to be efficient for default parameter choices in the bulk and
457 distortion energies, although some amount of tuning may be quite beneficial (particularly when changing
458 the distortion terms L_2 through L_6). The "Minimize" button performs the requested energy minimization
459 (either until a target force tolerance is attained or the maximum number of iterations is reached), with the
460 option to visualize the results only at the end or to watch the minimization proceed. The "File" dialog box
461 allows the currently visualized state of the system to be saved for separate analysis or processing.

462 Note that menu items allow any of the terms in the energy functional governing the simulation, Eq. 4, to
463 be changed at any moment. This allows, for example, the user to first minimize a system with some values
464 of the distortion constants and then perform repeated minimizations as those values are changed, observing
465 the stability or metastability of defect structures as this is done.

466 Two buttons allow the user to introduce boundaries and colloidal inclusions into the system. "Simple"
467 objects are spheres and flat walls with either normal homeotropic or degenerate planar anchoring conditions.
468 Arbitrarily complex boundary conditions (taking any shape, with degenerate planar and homeotropic
469 anchoring conditions not restricted by the direction of the surface normal) can be added by preparing a
470 simple text file that the program can read in – an example script that generates the custom boundary file
471 used in Fig. 1 is included in the "/tools" directory of Ref. [67].

472 With boundaries and colloids ("objects") in place, [some manipulations of these objects are accessible
via drop-down menus](#). The positions of these objects within the simulation can be directly modified, so
473 the user could place an ellipsoidal particle, perform a minimization, change the position, re-minimize the
474 system, and record the different energy minima attained. We include an option to automate this type of
475 operation (which can be used to build up the potential of mean force from the liquid crystal and colloid
476 interactions) for convenience. A near-term addition will be allowing objects to move according to the
477 integrated stresses at their surface (or according to the energetic results of various trial moves); the user
478 will then be able to separately "Minimize" just the liquid crystal sites or "Evolve [the] system" by allowing
479 both liquid crystalline and colloidal degrees of freedom to change simultaneously.

481 Finally, to facilitate moving from GUI prototyping to larger-scale MPI studies, we have included the
482 ability to record system initialization and sequences of commands entered in the graphical user interface,
483 and then save this sequence of commands as a new file that can be separately compiled and executed in
484 non-GUI operation. This file has its own set of command line options, primarily so that it can be made to
485 work as an MPI executable and so that the system size of the simulation it represents can be rescaled to a
486 larger value. We highlight this GUI-prototyping approach as a visual alternative to the scripting-language
487 approaches of molecular-dynamics packages like LAMMPS [91] or HOOMD-blue [92] for specifying
488 complex sequences of system initialization, energy minimizations, and the introduction of objects, fields,
489 and boundary conditions. We believe that this seamless visual-prototyping-to-MPI-scalable pipeline will
490 be beneficial to researchers interested in accessing experimental-scale simulations.

6 DISCUSSION

491 As demonstrated in our sample study, *openQmin* utilizes MPI to enable LdG modeling at typical size scales
492 of experimental relevance, at the $\sim 10 \mu\text{m}$ range, with fast convergence enabled by the FIRE algorithm.
493 Besides the colloidal defect configurations [and patterned boundaries](#) discussed here, another immediate use
494 is for the study of cholesterics, where typically fewer than ten pitches can fit inside a simulation box using

495 a single processor, but using *openQmin* tens of pitches can be modeled. While it may not be realistic at
496 present to frequently conduct simulations with 10^3 processors, using *openQmin* on computer clusters will
497 facilitate demonstration of how numerical results scale with system size, allowing reasonable extrapolations
498 to experimental scales.

499 For modeling at the $\sim 1 \mu\text{m}$ range or smaller, *openQmin*'s combination of FIRE with GPU computing
500 offers a substantial speedup, enabling users to manipulate the simulated conditions in a GUI environment
501 and observe the change in energy-minimized configurations. The GUI is useful for running “real-time”
502 tests of proposed configurations which can then be modeled at larger scales with MPI.

503 Likewise, the GUI will also be useful to experimentalists in quickly identifying more optimal properties
504 of nematics, colloidal particles, boundaries, etc. in order to achieve targeted topological or self-assembled
505 configurations. In general, numerical modeling can aid experimental studies not only in developing
506 theoretical understanding of nematic structures and energy landscapes, but also in performing high-
507 throughput searches through these design spaces. For example, geometric compatibility conditions favoring
508 lock-and-key assembly of particles and patterned walls [21, 37], or particle design promoting assembly
509 into photonic crystals, can be optimized more efficiently in numerics, to help guide the increasingly
510 sophisticated uses of fabrication techniques such as photolithography and two-photon polymerization [93].
511 An ambitious but important direction for future development is therefore to efficiently explore design
512 parameter spaces in numerical modeling, possibly employing genetic algorithms and techniques from
513 machine learning.

514 There are some near-term directions for future development of *openQmin* that we anticipate will increase
515 the usefulness of this open-source software to the liquid crystals research community. An expanded library
516 of Q-initialization options will facilitate investigations of chiral liquid crystals, topologically entangled or
517 knotted defect configurations [11, 12, 13, 14], and periodic defect arrays [26, 94], for example. A major
518 advance would be adding a flow field coupled to Q by Beris-Edwards nematodynamics, for investigations
519 of microfluidic geometries and active nematics.

520 Incorporating motion of colloidal particles into the modeling is another area for useful developments.
521 In the experimental system, energy is minimized not only over Q but also over the positions and (if
522 applicable) orientations of colloidal particles. At present, *openQmin* takes these latter degrees of freedom
523 as input parameters, and a free energy landscape can be mapped either informally using the GUI or
524 more systematically on a computer cluster. Thus one desired future improvement is to allow overdamped
525 translation and rotation of colloidal particles within the program, downhill in the energy landscape,
526 based on trial moves or on estimated nematic elastic stresses felt by the particle [46]. The trial move
527 approach, requiring several re-minimizations of Q at each time step, is made less cumbersome by improved
528 convergence speed of the FIRE algorithm.

529 Finally, we hope that *openQmin*'s GUI interface will be useful in physics education. Interacting with
530 a fast and “hands-on” version of the numerical modeling, students at the undergraduate or beginning
531 graduate level can quickly gain experience and intuition for liquid crystals. This will help to capitalize
532 on the position of liquid crystals as one of the most accessible, and visualizable, physical realizations of
533 abstract topological ideas relevant to many areas of physics.

CONFLICT OF INTEREST STATEMENT

534 The authors declare that the research was conducted in the absence of any commercial or financial
535 relationships that could be construed as a potential conflict of interest.

AUTHOR CONTRIBUTIONS

536 DMS and DAB designed the study, developed the open-source software, and wrote the manuscript.

FUNDING

537 DMS was supported by NSF-POLS- 1607416 as well as Simons Foundation Grant Number 454947. The
538 Tesla K40s used for this research were donated by the NVIDIA Corporation. We acknowledge computing
539 support via an XSEDE allocation on Comet through Grant No. NSF-TG-PHY190027, [and from the](#)
540 [Multi-Environment Computer for Exploration and Discovery \(MERCED\) cluster at UC Merced](#), which
541 was funded by National Science Foundation Grant No. ACI-1429783.

ACKNOWLEDGMENTS

542 DAB thanks Gareth Alexander for introducing him to LdG numerical modeling, and gratefully
543 acknowledges illuminating discussions with Simon Čopar, Miha Ravnik, and Slobodan Žumer.

DATA AVAILABILITY STATEMENT

544 The open source code described in this work can be found at Ref. [67] and used to reproduce all data in the
545 manuscript. Documentation for the software is maintained at [95], [and can also be generated with doxygen](#)
546 [from the source code](#).

REFERENCES

- 547 [1] Friedel G. Les états mésomorphes de la matière. *Annales de Physique* **18** (1922) 273–474.
- 548 [2] Poulin P, Stark H, Lubensky T, Weitz D. Novel colloidal interactions in anisotropic fluids. *Science*
549 **275** (1997) 1770–1773.
- 550 [3] Dickson W, Wurtz GA, Evans PR, Pollard RJ, Zayats AV. Electronically controlled surface plasmon
551 dispersion and optical transmission through metallic hole arrays using liquid crystal. *Nano Letters* **8**
552 (2008) 281–286.
- 553 [4] Liu Q, Cui Y, Gardner D, Li X, He S, Smalyukh II. Self-alignment of plasmonic gold nanorods in
554 reconfigurable anisotropic fluids for tunable bulk metamaterial applications. *Nano Letters* **10** (2010)
555 1347–1353.
- 556 [5] Wang X, Miller DS, Bukusoglu E, De Pablo JJ, Abbott NL. Topological defects in liquid crystals as
557 templates for molecular self-assembly. *Nature Materials* **15** (2016) 106.
- 558 [6] Rodarte AL, Pandolfi RJ, Ghosh S, Hirst LS. Quantum dot/liquid crystal composite materials: self-
559 assembly driven by liquid crystal phase transition templating. *Journal of Materials Chemistry C* **1**
560 (2013) 5527–5532.
- 561 [7] Rodarte A, Cisneros F, Hein J, Ghosh S, Hirst L. Quantum dot/liquid crystal nanocomposites in
562 photonic devices. *Photonics* (Multidisciplinary Digital Publishing Institute) (2015), vol. 2, 855–864.
- 563 [8] Muševič I, Škarabot M, Tkalec U, Ravnik M, Žumer S. Two-dimensional nematic colloidal crystals
564 self-assembled by topological defects. *Science* **313** (2006) 954–958.
- 565 [9] Mundoor H, Senyuk B, Smalyukh II. Triclinic nematic colloidal crystals from competing elastic and
566 electrostatic interactions. *Science* **352** (2016) 69–73.
- 567 [10] Nych A, Ognysta U, Škarabot M, Ravnik M, Žumer S, Muševič I. Assembly and control of 3D
568 nematic dipolar colloidal crystals. *Nature Communications* **4** (2013) 1489.

- 569 [11] Ravnik M, Škarabot M, Žumer S, Tkalec U, Poberaj I, Babič D, et al. Entangled nematic colloidal
570 dimers and wires. *Physical Review Letters* **99** (2007) 247801.
- 571 [12] Tkalec U, Ravnik M, Čopar S, Žumer S, Mušević I. Reconfigurable knots and links in chiral nematic
572 colloids. *Science* **333** (2011) 62–5. doi:10.1126/science.1205705.
- 573 [13] Tasinkevych M, Campbell MG, Smalyukh II. Splitting, linking, knotting, and solitonic escape of
574 topological defects in nematic drops with handles. *Proceedings of the National Academy of Sciences*
575 **111** (2014) 16268–16273.
- 576 [14] Machon T, Alexander GP. Knotted defects in nematic liquid crystals. *Physical Review Letters* **113**
577 (2014) 027801.
- 578 [15] Ravnik M, Alexander GP, Yeomans JM, Žumer S. Three-dimensional colloidal crystals in liquid
579 crystalline blue phases. *Proceedings of the National Academy of Sciences* **108** (2011) 5188–92.
580 doi:10.1073/pnas.1015831108.
- 581 [16] Lavrentovich OD. Liquid crystals, photonic crystals, metamaterials, and transformation optics.
582 *Proceedings of the National Academy of Sciences* **108** (2011) 5143–5144.
- 583 [17] Humar M, Mušević I. 3D microlasers from self-assembled cholesteric liquid-crystal microdroplets.
584 *Optics Express* **18** (2010) 26995–27003.
- 585 [18] Mušević I. Interactions, topology and photonic properties of liquid crystal colloids and dispersions.
586 *The European Physical Journal Special Topics* **227** (2019) 2455–2485.
- 587 [19] Serra F. Curvature and defects in nematic liquid crystals. *Liquid Crystals* **43** (2016) 1920–1936.
- 588 [20] Hung FR, Gettelfinger BT, Koenig Jr GM, Abbott NL, de Pablo JJ. Nanoparticles in nematic liquid
589 crystals: Interactions with nanochannels. *The Journal of chemical physics* **127** (2007) 124702.
- 590 [21] Eskandari Z, Silvestre N, da Gama MT, Ejtehadi M. Particle selection through topographic templates
591 in nematic colloids. *Soft Matter* **10** (2014) 9681–9687.
- 592 [22] Luo Y, Serra F, Stebe KJ. Experimental realization of the “lock-and-key” mechanism in liquid crystals.
593 *Soft matter* **12** (2016) 6027–6032.
- 594 [23] Guillamat P, Sagués F, Ignés-Mullol J. Electric-field modulation of liquid crystal structures in contact
595 with structured surfactant monolayers. *Physical Review E* **89** (2014) 052510.
- 596 [24] Kos Ž, Ravnik M. Relevance of saddle-splay elasticity in complex nematic geometries. *Soft Matter*
597 **12** (2016) 1313–1323.
- 598 [25] Peng C, Guo Y, Conklin C, Viñals J, Shiyanovskii SV, Wei QH, et al. Liquid crystals with patterned
599 molecular orientation as an electrolytic active medium. *Physical Review E* **92** (2015) 052502.
- 600 [26] Murray BS, Pelcovits RA, Rosenblatt C. Creating arbitrary arrays of two-dimensional topological
601 defects. *Physical Review E* **90** (2014) 052501.
- 602 [27] Williams C, Cladis P, Kleman M. Screw disclinations in nematic samples with cylindrical symmetry.
603 *Molecular Crystals and Liquid Crystals* **21** (1973) 355–373.
- 604 [28] Volovik G, Lavrentovich O. Topological dynamics of defects: boojums in nematic drops. *Zh Eksp
605 Teor Fiz* **85** (1983) 1997–2010.
- 606 [29] Nelson DR. Toward a tetravalent chemistry of colloids. *Nano Letters* **2** (2002) 1125–1129.
- 607 [30] Lavrentovich O, Nastishin YA. Defects in degenerate hybrid aligned nematic liquid crystals. *EPL
608 (Europhysics Letters)* **12** (1990) 135.
- 609 [31] Wright DC, Mermin ND. Crystalline liquids: the blue phases. *Reviews of Modern Physics* **61** (1989)
610 385.
- 611 [32] Alama S, Bronsard L, Lamy X. Minimizers of the landau–de gennes energy around a spherical colloid
612 particle. *Archive for Rational Mechanics and Analysis* **222** (2016) 427–450.

- 613 [33] Alama S, Bronsard L, Lamy X. Analytical description of the saturn-ring defect in nematic colloids.
614 *Physical Review E* **93** (2016) 012705.
- 615 [34] Kralj S, Žumer S. Fréedericksz transitions in supra-um nematic droplets. *Physical Review A* **45** (1992)
616 2461–2470.
- 617 [35] Tkalec U, Škarabot M, Muševič I. Interactions of micro-rods in a thin layer of a nematic liquid crystal.
618 *Soft Matter* **4** (2008) 2402–2409.
- 619 [36] Emeršič T, Zhang R, Kos Ž, Čopar S, Osterman N, de Pablo JJ, et al. Sculpting stable structures in
620 pure liquids. *Science Advances* **5** (2019) eaav4283.
- 621 [37] Luo Y, Beller DA, Boniello G, Serra F, Stebe KJ. Tunable colloid trajectories in nematic liquid crystals
622 near wavy walls. *Nature Communications* **9** (2018) 3841.
- 623 [38] Tasinkevych M, Mondiot F, Mondain-Monval O, Loudet JC. Dispersions of ellipsoidal particles in a
624 nematic liquid crystal. *Soft Matter* **10** (2014) 2047–2058.
- 625 [39] Hashemi SM, Ejtehadi MR. Equilibrium state of a cylindrical particle with flat ends in nematic liquid
626 crystals. *Physical Review E* **91** (2015) 012503.
- 627 [40] Hung F, Bale S. Faceted nanoparticles in a nematic liquid crystal: defect structures and potentials of
628 mean force. *Molecular Simulation* **35** (2009) 822–834.
- 629 [41] Hung FR. Quadrupolar particles in a nematic liquid crystal: Effects of particle size and shape. *Physical
630 Review E* **79** (2009) 021705.
- 631 [42] Hung FR, Guzmán O, Gettelfinger BT, Abbott NL, de Pablo JJ. Anisotropic nanoparticles immersed
632 in a nematic liquid crystal: Defect structures and potentials of mean force. *Physical Review E* **74**
633 (2006) 011711.
- 634 [43] Beller DA, Gharbi MA, Liu IB. Shape-controlled orientation and assembly of colloids with sharp
635 edges in nematic liquid crystals. *Soft Matter* **11** (2015) 1078–1086.
- 636 [44] Araki T, Tanaka H. Colloidal aggregation in a nematic liquid crystal: topological arrest of particles by
637 a single-stroke disclination line. *Physical Review Letters* **97** (2006) 127801.
- 638 [45] Škarabot M, Ravnik M, Žumer S, Tkalec U, Poberaj I, Babič D, et al. Interactions of quadrupolar
639 nematic colloids. *Physical Review E* **77** (2008) 031705.
- 640 [46] Škarabot M, Ravnik M, Žumer S, Tkalec U, Poberaj I, Babič D, et al. Hierarchical self-assembly of
641 nematic colloidal superstructures. *Physical Review E* **77** (2008) 061706.
- 642 [47] Ravnik M, Žumer S. Landau–de Gennes modelling of nematic liquid crystal colloids. *Liquid Crystals*
643 **36** (2009) 1201–1214.
- 644 [48] Mori H, Gartland EC, Kelly JR, Box PJ. Multidimensional director modeling using the Q tensor repre-
645 sentation in a liquid crystal cell and its application to the π cell with patterned electrodes. *Jap. J. App.
646 Phys* **38** (1999) 135.
- 647 [49] Beris AN, Edwards BJ. *Thermodynamics of flowing systems: with internal microstructure* (Oxford
648 University Press) (1994).
- 649 [50] Qian T, Sheng P. Generalized hydrodynamic equations for nematic liquid crystals. *Physical Review E*
650 **58** (1998) 7475.
- 651 [51] Denniston C, Orlandini E, Yeomans J. Lattice Boltzmann simulations of liquid crystal hydrodynamics.
652 *Physical Review E* **63** (2001) 056702.
- 653 [52] Spencer T, Care C. Lattice boltzmann scheme for modeling liquid-crystal dynamics: Zenithal bistable
654 device in the presence of defect motion. *Physical Review E* **74** (2006) 061708.
- 655 [53] Carenza LN, Gonnella G, Lamura A, Negro G, Tiribocchi A. Lattice Boltzmann Methods and Active
656 Fluids. *arXiv e-prints* (2019) arXiv:1906.01129.

- 657 [54] Marenduzzo D, Orlandini E, Cates M, Yeomans J. Steady-state hydrodynamic instabilities of active
658 liquid crystals: Hybrid lattice Boltzmann simulations. *Physical Review E* **76** (2007) 031921.
- 659 [55] Cates M, Henrich O, Marenduzzo D, Stratford K. Lattice Boltzmann simulations of liquid crystalline
660 fluids: active gels and blue phases. *Soft Matter* **5** (2009) 3791–3800.
- 661 [56] Lee KW, Mazza MG. Stochastic rotation dynamics for nematic liquid crystals. *The Journal of
662 Chemical Physics* **142** (2015) 164110.
- 663 [57] Shendruk TN, Yeomans JM. Multi-particle collision dynamics algorithm for nematic fluids. *Soft
664 Matter* **11** (2015) 5101–5110.
- 665 [58] Mandal S, Mazza MG. Multiparticle collision dynamics for tensorial nematodynamics. *Physical
666 Review E* **99** (2019) 063319.
- 667 [59] James R, Willman E, Fernandez FA, Day SE. Computer modeling of liquid crystal hydrodynamics.
668 *IEEE Transactions on Magnetics* **44** (2008) 814–817.
- 669 [60] Giomi L, Mahadevan L, Chakraborty B, Hagan M. Excitable patterns in active nematics. *Physical
670 Review Letters* **106** (2011) 218101.
- 671 [61] Svenšek D, Žumer S. Hydrodynamics of pair-annihilating disclination lines in nematic liquid crystals.
672 *Physical Review E* **66** (2002) 021712.
- 673 [62] Terentjev E. Disclination loops, standing alone and around solid particles, in nematic liquid crystals.
674 *Physical Review E* **51** (1995) 1330.
- 675 [63] Stark H. Physics of colloidal dispersions in nematic liquid crystals. *Physics Reports* **351** (2001)
676 387–474.
- 677 [64] Gharbi MA, Cavallaro Jr M, Wu G, Beller DA, Kamien RD, Yang S, et al. Microbullet assembly:
678 interactions of oriented dipoles in confined nematic liquid crystal. *Liquid Crystals* **40** (2013) 1619–
679 1627.
- 680 [65] Luo Y, Yao T, Beller DA, Serra F, Stebe KJ. Deck the walls with anisotropic colloids in nematic liquid
681 crystals. *Langmuir* (2019).
- 682 [66] Bajc I, Hecht F, Žumer S. A mesh adaptivity scheme on the Landau–de Gennes functional minimization
683 case in 3D, and its driving efficiency. *Journal of Computational Physics* **321** (2016) 981–996.
- 684 [67] Sussman D, Beller D. <https://github.com/sussmanlab/open-qmin> (2019).
- 685 [68] Gabriel E, Fagg GE, Bosilca G, Angskun T, Dongarra JJ, Squyres JM, et al. Open mpi: Goals, concept,
686 and design of a next generation mpi implementation. *European Parallel Virtual Machine/Message
687 Passing Interface Users' Group Meeting* (Springer) (2004), 97–104.
- 688 [69] de Gennes PG, Prost J. *The Physics of Liquid Crystals* (Clarendon Press), second edn. (1993).
- 689 [70] Mottram NJ, Newton CJ. Introduction to Q-tensor theory. *arXiv preprint arXiv:1409.3542* (2014).
- 690 [71] Schophol N, Sluckin TJ. Defect core structure in nematic liquid crystals. *Physical Review Letters* **59**
691 (1987) 2582.
- 692 [72] Jeu WHD, Claassen WAP, Spruijt AMJ. The determination of the elastic constants of nematic liquid
693 crystals. *Molecular Crystals and Liquid Crystals* **37** (1976) 269–280.
- 694 [73] Madhusudana NV, Pratibha R. Elasticity and orientational order in some cyanobiphenyls: Part iv.
695 reanalysis of the data. *Molecular Crystals and Liquid Crystals* **89** (1982) 249–257.
- 696 [74] Poniewierski A, Sluckin T. On the free energy density of non-uniform nematics. *Molecular Physics*
697 **55** (1985) 1113–1127.
- 698 [75] Rapini A, Papoulier M. Distorsion d'une lamelle nématische sous champ magnétique conditions
699 d'ancre aux parois. *Le Journal de Physique Colloques* **30** (1969) C4–54.
- 700 [76] Nobili M, Durand G. Disorientation-induced disordering at a nematic-liquid-crystal-solid interface.
701 *Physical Review A* **46** (1992) R6174.

- 702 [77] Fournier JB, Galatola P. Modeling planar degenerate wetting and anchoring in nematic liquid crystals.
703 *EPL (Europhysics Letters)* **72** (2005) 403.
- 704 [78] Nvidia C. Nvidia CUDA C programming guide. *Nvidia Corporation* **120** (2011) 8.
- 705 [79] Noye B, Arnold R. Accurate finite difference approximations for the Neumann condition on a curved
706 boundary. *Applied Mathematical Modelling* **14** (1990) 2–13.
- 707 [80] Nocedal J, Wright S. *Numerical Optimization* (Springer Science & Business Media) (2006).
- 708 [81] Bitzek E, Koskinen P, Gähler F, Moseler M, Gumbsch P. Structural relaxation made simple. *Physical
709 Review Letters* **97** (2006) 170201.
- 710 [82] Polyak BT. Some methods of speeding up the convergence of iteration methods. *USSR Computational
711 Mathematics and Mathematical Physics* **4** (1964) 1–17.
- 712 [83] Sheppard D, Terrell R, Henkelman G. Optimization methods for finding minimum energy paths. *The
713 Journal of Chemical Physics* **128** (2008) 134106.
- 714 [84] Herbol HC, Stevenson J, Clancy P. Computational implementation of nudged elastic band, rigid
715 rotation, and corresponding force optimization. *Journal of Chemical Theory and Computation* **13**
716 (2017) 3250–3259.
- 717 [85] Zhou Y, Moseler M, Müser MH. Solution of boundary-element problems using the fast-inertial-
718 relaxation-engine method. *Physical Review B* **99** (2019) 144103.
- 719 [86] Wang Y, Jia Z, Wen Z. The search direction correction makes first-order methods faster. *arXiv preprint
720 arXiv:1905.06507* (2019).
- 721 [87] Lulli M, Bernaschi M, Parisi G. Highly optimized simulations on single-and multi-gpu systems of the
722 3D Ising spin glass model. *Computer Physics Communications* **196** (2015) 290–303.
- 723 [88] Gu Y, Abbott NL. Observation of saturn-ring defects around solid microspheres in nematic liquid
724 crystals. *Physical Review Letters* **85** (2000) 4719.
- 725 [89] Loudet J, Poulin P. Application of an electric field to colloidal particles suspended in a liquid-crystal
726 solvent. *Physical Review Letters* **87** (2001) 165503.
- 727 [90] Lubensky T, Pettey D, Currier N, Stark H. Topological defects and interactions in nematic emulsions.
728 *Physical Review E* **57** (1998) 610.
- 729 [91] Plimpton S. Fast parallel algorithms for short-range molecular dynamics. *Journal of Computational
730 Physics* **117** (1995) 1–19.
- 731 [92] Anderson JA, Lorenz CD, Travesset A. General purpose molecular dynamics simulations fully
732 implemented on graphics processing units. *Journal of Computational Physics* **227** (2008) 5342–5359.
- 733 [93] Martinez A, Ravnik M, Lucero B, Visvanathan R, Žumer S, Smalyukh II. Mutually tangled colloidal
734 knots and induced defect loops in nematic fields. *Nature Materials* (2014).
- 735 [94] Suh A, Gim MJ, Beller D, Yoon DK. Topological defects and geometric memory across the nematic-
736 smectic a liquid crystal phase transition. *Soft Matter* (2019).
- 737 [95] Sussman D, Beller D. <https://dmsussman.gitlab.io/landaudegui/> (2019).

FIGURE CAPTIONS

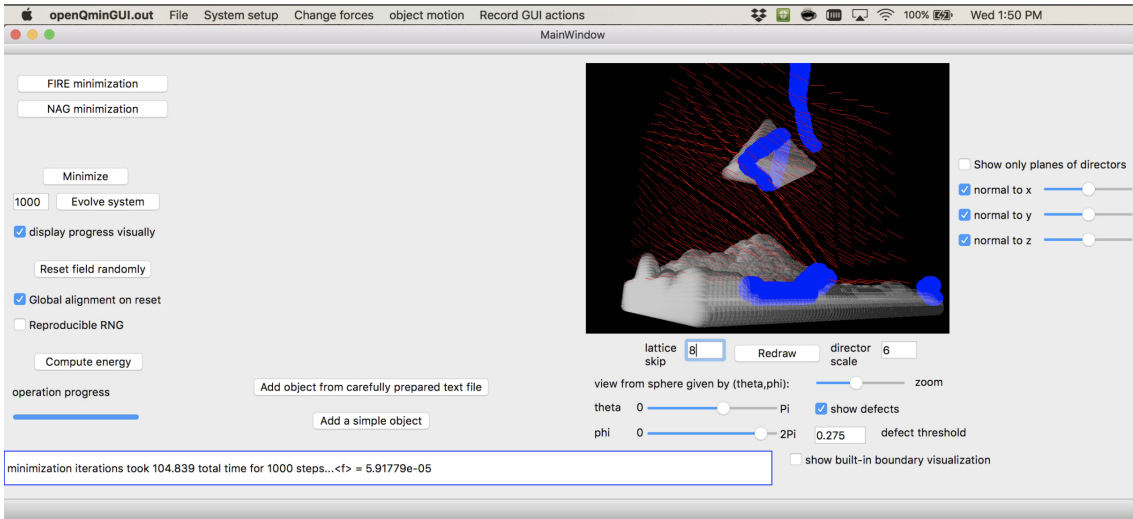


Figure 1. Snapshot of the graphical user interface provided by *openQmin*, here shown simulating the defect structure near a pyramidal colloid above a topographically nontrivial boundary, all with oriented anchoring along user-specified directions to approximately model homeotropic surfaces.

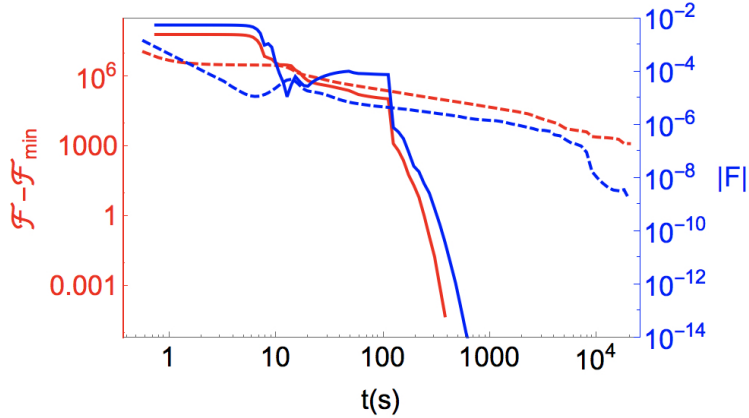


Figure 2. (Red) Energy relative to the uniform texture with preferred nematic order, $\mathcal{F} - \mathcal{F}_{min}$, and (blue) the norm of the residual force vector, $|F|/\sqrt{N}$, for bulk nematic (lattice size is $N = 250^3$), starting from a randomly initialized configuration, as a function of wall-clock time. Solid lines are minimizations using FIRE and dashed lines are those using gradient descent. As described in the text, we have tuned the minimization parameters (step size, etc.) for each algorithm separately and use identical hardware to make a one-to-one comparison.

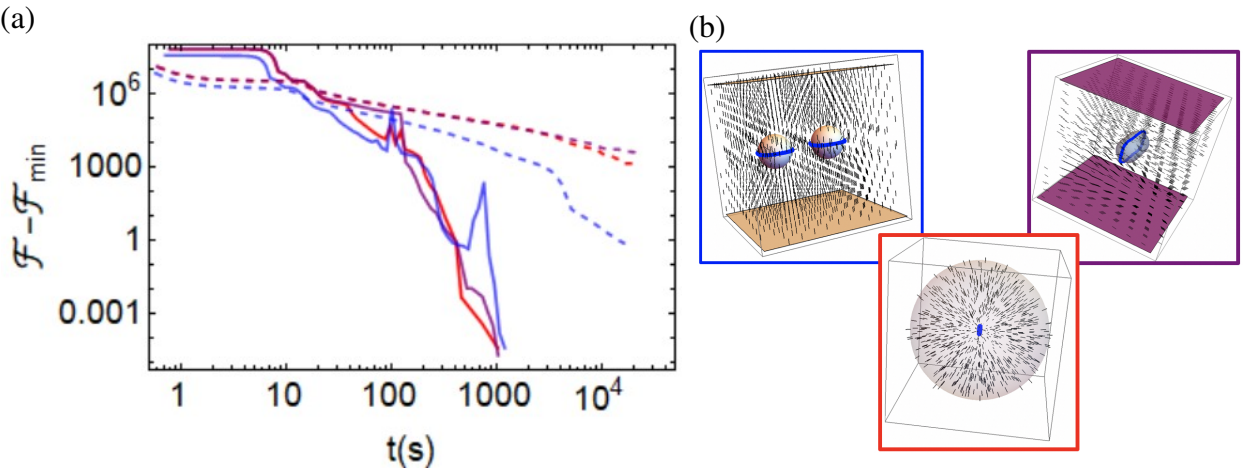


Figure 3. (a) Energy relative to the minimized energy for three different geometries as a function of wall-clock time, in a lattice of size $N = 250^3$ and starting from a randomly initialized configuration. As in Fig. 2, solid lines are minimizations using FIRE and dashed lines are those using gradient descent. As depicted in (b) showing the minimized configurations, the three sets of lines correspond to (Blue) two spherical colloids between parallel plates, all with homeotropic anchoring, (Red) the interior of a spherical droplet with homeotropic anchoring, and (Purple) a spherocylinder with homeotropic anchoring between parallel plates with planar degenerate anchoring. [These images were created using the “multirankImages.nb” Mathematica file included in the repository for making simple visualizations.](#)

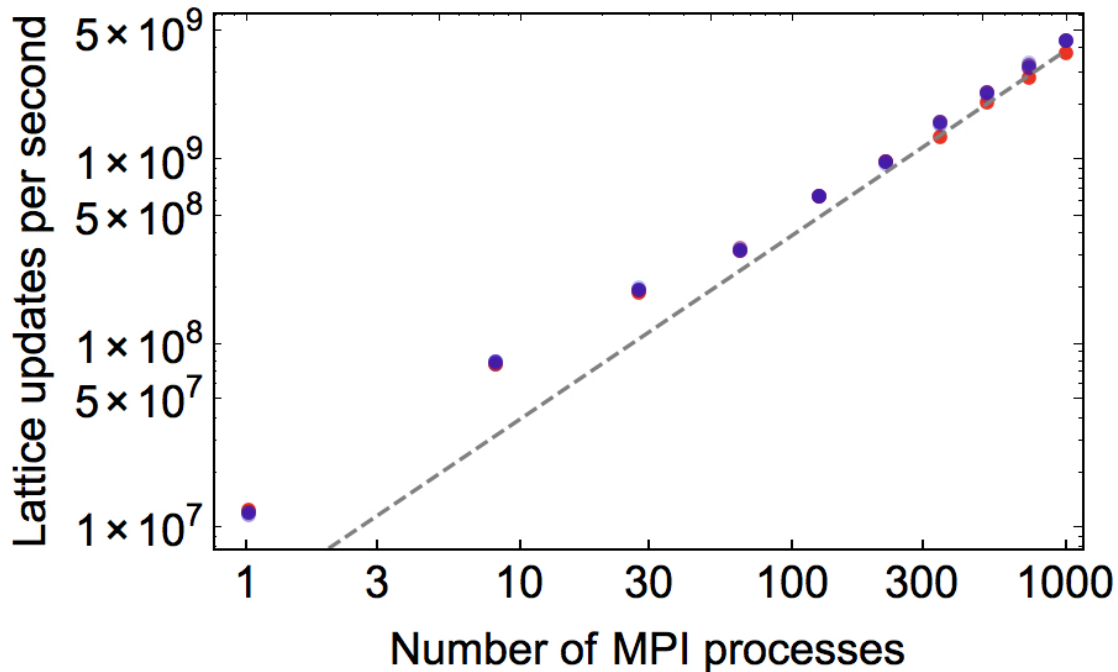


Figure 4. Weak scaling performance of *openQmin* on Comet, in total number of lattice site updates (i.e., (time steps) \times (ranks) \times (N_p)) per second vs. the number of CPU processes, P , for a constant number of lattice sites per process. The points from dark red to light blue correspond to $N_p = 75^3, 100^3, 125^3, 150^3, 250^3$ lattice sites per rank. The dashed gray line corresponds to ideal $\propto P$ scaling.

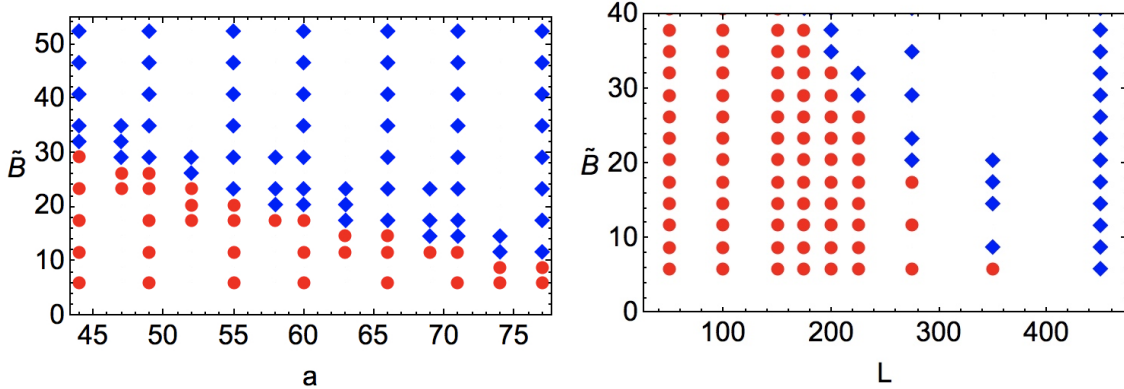
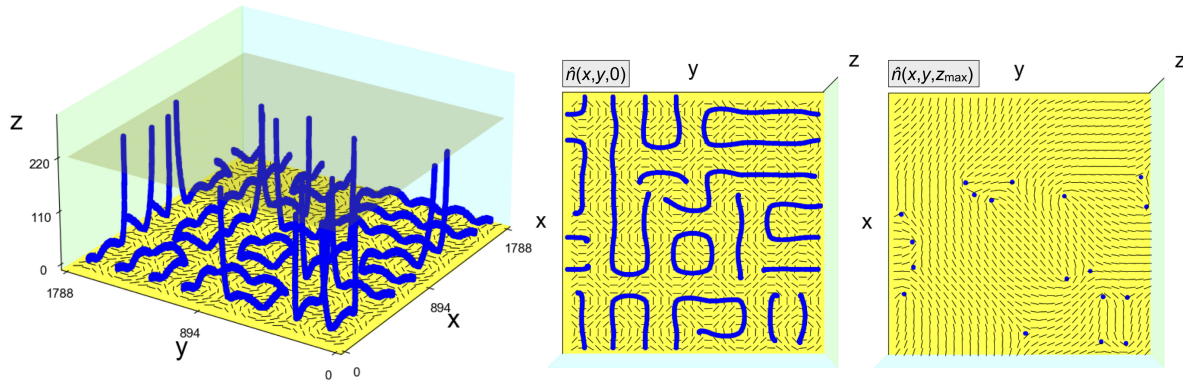
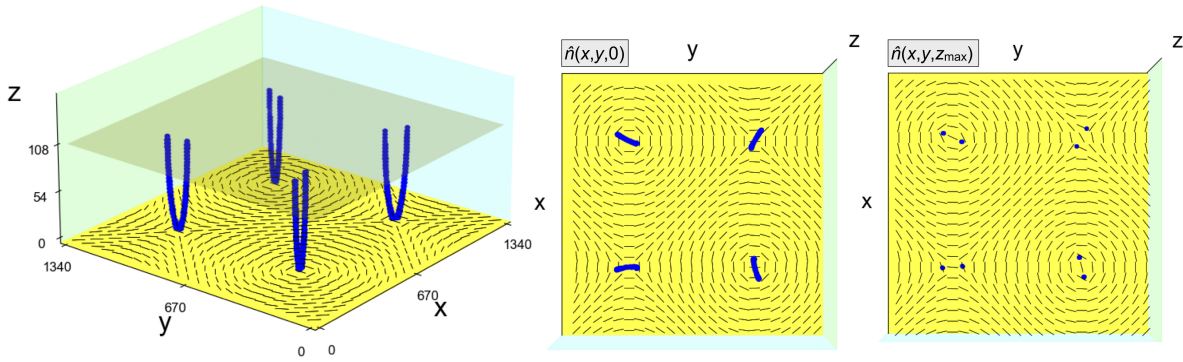


Figure 5. Stability of dipolar defects around a spherical colloidal inclusion at fixed $S_0 = 0.53$ as a function of dimensionless [bulk free energy density](#) constant \tilde{B} , colloid size a , and linear system size L , with a and L in units of the lattice spacing. Regions of parameter space with meta-stable dipolar configurations are shown with blue diamonds, stable quadrupolar configurations are shown with red circles. (Left) For fixed lattice size of $N = 275^3$, we vary the dimensionless [bulk free energy density](#) constant \tilde{B} and the colloidal radius a . (Right) For fixed ratio of colloidal radius to linear system size, $a = 0.22 \times L = 0.22 \times N^{1/3}$, we vary \tilde{B} and L . Particularly for the larger values of a , one can see dependence of hedgehog meta-stability on L , indicating the importance of far-field distortions and boundary conditions (here, periodic).

(a)



(b)



(c)

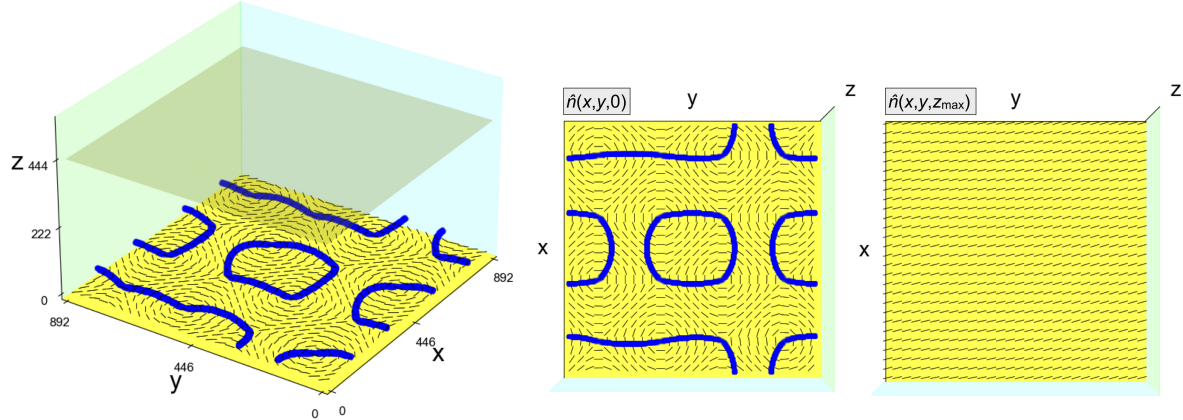


Figure 6. Numerically computed disclination configurations near planar substrates patterned with square arrays of alternating ± 1 surface disclinations. The opposite planar boundary (transparent square) has degenerate planar anchoring. (a) An 8x8 array of surface disclinations with spacing equal to the cell thickness. (b) A 2x2 array of surface disclinations with spacing equal to six times the cell thickness. (c) A 4x4 array of surface disclinations with spacing equal to half the cell thickness. Configurations in (a)-(c) are partially energy-minimized. Disclinations are colored blue. Axes values are given in units of the lattice spacing. In each row, the second panel shows a top view of the disclinations in bulk and the director field in the plane of the patterned substrate; the third panel shows a top view of the director field on the opposite surface, along with the half-integer disclination points (if any) in that surface. These images are made using the “visualize.py” Python script included in the repository for taking saved configurations and making simple visualizations from the command line.